Nano Research

Open Access

Research Article

Synthesis of wafer-scale monolayer MoS_2 on sapphire: Unlocking the influence of key growth parameters

Rong Song[1,§], Dingyi Shen[2,§], Dongyan Liu[1], Jingyi Liang[1], Zimei Zhang[1], Jingmei Tang[1], Liang Chen[1], Bo Li[3], Jia Li[1]✉, and Xidong Duan[1]✉

[1] *Hunan Key Laboratory of Two-Dimensional Materials, State Key Laboratory for Chemo/ Biosensing and Chemometrics, College of Chemistry and Chemical Engineering, Chongqing Research Institute, Hunan University, Changsha 410082, China*
[2] *Hubei Key Laboratory of Energy Storage and Power Battery, School of Mathematics, Physics and Optoelectronic Engineering, Hubei University of Automotive Technology, Shiyan 442002, China*
[3] *College of Semiconductors (College of Integrated Circuits), Hunan University, Changsha 410082, China*
§ *Rong Song and Dingyi Shen contributed equally to this work.*

Cite this article: *Nano Research*, **2025**, *18*, 94907140. https://doi.org/10.26599/NR.2025.94907140

ABSTRACT: Large-scale synthesis of high-quality two-dimensional (2D) semiconductors, such as molybdenum disulfide (MoS_2), is a prerequisite for their lab-to-fab transition. It is crucial to systematically explore and understand the influence of key synthetic conditions on the nucleation, uniformity, and quality of MoS_2 wafers. Here, we report the epitaxial growth of high-quality and uniform monolayer MoS_2 films on 2-in c-plane sapphire by chemical vapor deposition (CVD) method under optimized growth conditions (0–1 mg NaCl, adequate S/Mo ratio, and the addition of 0–1 sccm O_2). We systematically explore the influence of critical synthetic conditions on the nucleation, and stitching of MoS_2 domains over the wafer scale, including the dosage of the alkali metal salt NaCl additive, the evaporation temperature of MoO_3, the distance between MoO_3 and the substrate, and the flow rate of O_2. Among them, the dosage of NaCl and the S/Mo ratio have important influences on the quality and film coverage of MoS_2, while the flow rate of O_2 plays a key role in controlling the nucleation density and domain size. We further discovered that a-plane sapphire could easily guide the unidirectional growth of MoS_2 without the need for other specific synthetic conditions compared with c-plane and m-plane sapphire. The field-effect transistors (FETs) fabricated from the full-coverage films show an average and the highest mobilities of 28.5 and around 45 $cm^2 \cdot V^{-1} \cdot s^{-1}$, respectively.

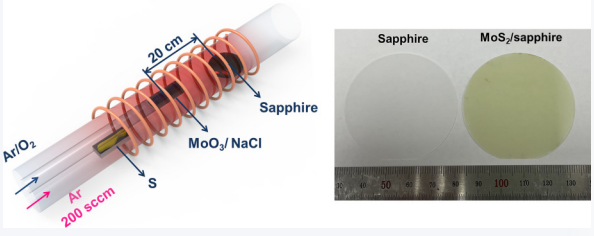

KEYWORDS: wafer-scale MoS_2 films, chemical vapor deposition, critical synthetic conditions, monolayer, field-effect transistors

1 Introduction

Monolayer MoS_2 is a promising two-dimensional (2D) semiconductor material for high-performance electronics and optoelectronics due to its atomically thin thickness, high mobility, excellent gate controllability, high current switching ratio, and low dielectric constant [1–7]. Specifically, monolayer MoS_2 transistors with sub-1-nm gate lengths [8] or channel lengths below 1 nm [9] have been successfully demonstrated, suggesting the great potential of MoS_2 in next-generation ultra-scale electronics [10–15]. To explore the full potential of MoS_2 in high-end industrial applications, it is critical to prepare high-quality wafer-scale uniform monolayer MoS_2 films. To date, various chemical synthesis approaches have been used to achieve this goal, such as chemical vapor deposition (CVD) [16–19], metal-organic CVD (MOCVD) [20–22], and atomic layer deposition (ALD) [23–25]. Among these methods, the CVD method stands out as one of the most compelling growth methods for the scalable production of high-quality MoS_2 [26–30]. This method is synergistically controlled by many factors such as vapor pressure, temperature of the precursor materials, substrate properties, and temperature. Additionally, in a practical growth apparatus, a slight variation of the local conditions (for example, temperature gradient or vapor pressure gradient) could lead to spatial fluctuations in supersaturation at different locations, resulting in non-uniform growth. Much progress has

Received: September 26, 2024; **Revised:** November 2, 2024
Accepted: November 18, 2024

✉Address correspondence to Jia Li, jiali2@hnu.edu.cn; Xidong Duan, xidongduan@hnu.edu.cn

been made regarding the growth of MoS_2 wafers, but the detail optimization process is always ignored or simplified.

Sapphire, a well-developed commercial substrate, has good thermal stability, small deformation, smooth surface, and good lattice matching with MoS_2, which is widely used in the preparation of wafer-scale 2D semiconducting films [31–37]. The substrate design also plays a key role in producing unidirectional MoS_2 domains and single-crystal films, which can greatly reduce grain boundaries and improve film quality [38–41]. For example, wafer-scale single crystal MoS_2 [42] and WS_2 [43] films were synthesized on carefully designed C/A-1° and a-plane sapphire, respectively. The obtained wafer-scale MoS_2 films on sapphire also exhibit high optical and electrical qualities, with the highest carrier mobility up to 140 $cm^2 \cdot V^{-1} \cdot s^{-1}$ [38, 44]. To explore the full potential of monolayer MoS_2, it is crucial to systematically explore and understand the influence of key synthetic conditions on the nucleation, uniformity, and quality of MoS_2 wafers on sapphire substrate.

In this work, we successfully prepared 2-in monolayer MoS_2 films on sapphire (c-face with a miscut of ~ 0.2°) by CVD process. We systematically explored the influence of critical synthetic conditions on the nucleation, and stitching of MoS_2 domains over the wafer scale, the optimized growth conditions are 0–1 mg NaCl, the evaporation temperature of MoO_3 is 530–580 °C, the optimized distance is 16–23 cm, and the flow rate of O_2 is 0–1 sccm. Especially, the dosage of NaCl and the S/Mo ratio have important influences on the quality and film coverage of MoS_2, while the flow rate of O_2 plays a key role in controlling the nucleation density and domain size. In addition, we found that a-plane sapphire can easily guide the unidirectional growth of MoS_2, compared with c-plane and m-plane sapphire. Microscopy and spectroscopy characterization demonstrate the high quality of the synthesized wafer-scale MoS_2 films. The field-effect transistors (FETs) fabricated from the as-grown films show an average and the highest mobilities of 28.5 and around 45 $cm^2 \cdot V^{-1} \cdot s^{-1}$, respectively. This study provides a practical reference for the growth of wafer-scale MoS_2 films.

2 Results and discussion

2.1 Growth and characterization of wafer-scale monolayer MoS_2 films

The growth of monolayer MoS_2 films on sapphire was conducted in a low-pressure CVD system with a three-zone tube furnace (Fig. 1(a)). MoO_3 and S powder were selected as precursors. MoO_3 was placed in an independent quartz tube in the growth chamber (zone I), and the carrier gas was Ar/O_2 (100/1 sccm). S (zone I) and substrates (zone III) were directly placed in the growth chamber with 200 sccm Ar. Figure 1(a) shows the CVD system and several critical parameters in the wafer material growth process, including the dosage of the alkali metal salt NaCl, the evaporation temperature of MoO_3, the distance between MoO_3 and the substrate, and the flow rate of O_2. Figure 1(b) shows the as-grown

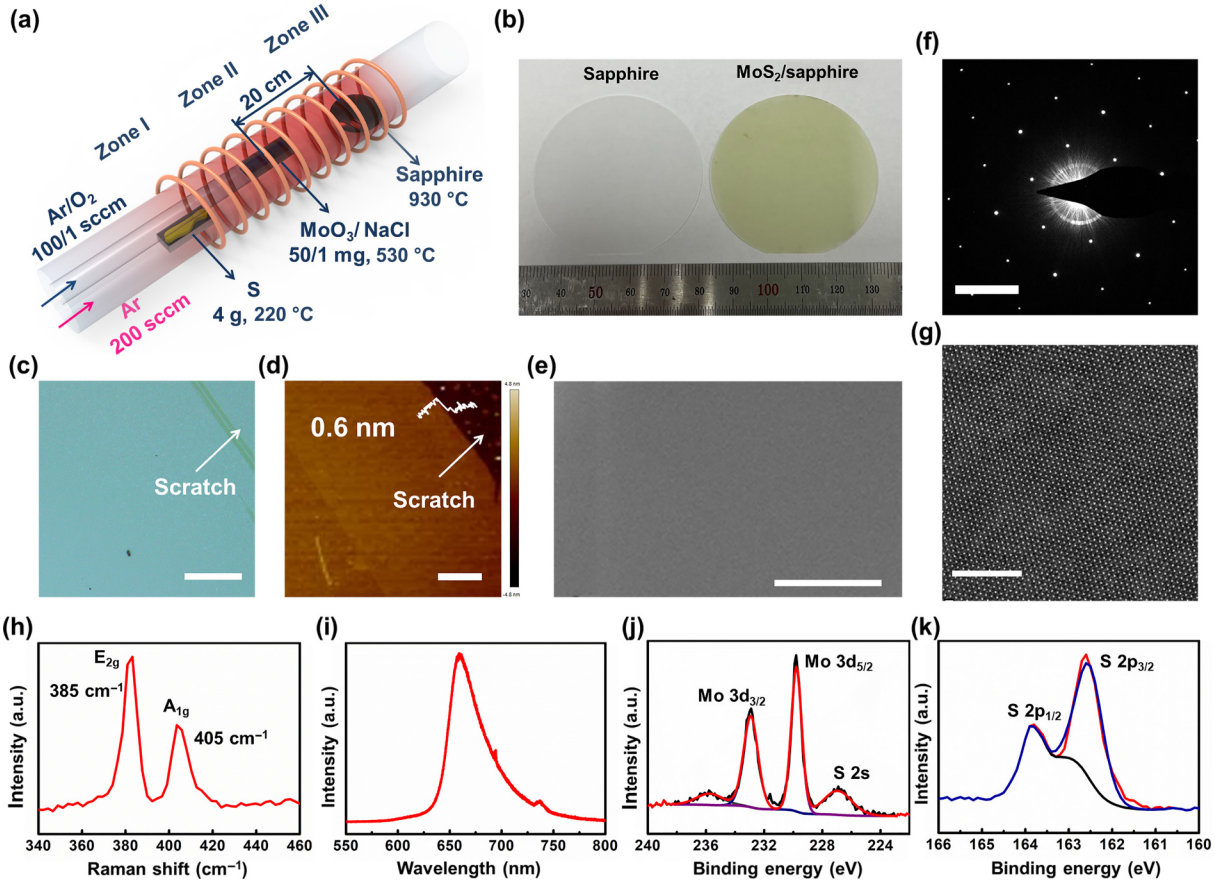

Figure 1 Growth and characterization of monolayer MoS_2 film on sapphire. (a) Schematic illustrations of the critical parameters for the synthesis of 2-in monolayer (1L) MoS_2 film. (b) Photograph of a 2-in sapphire substrate (left) and after monolayer MoS_2 growth (right). (c) OM images of MoS_2 grown on sapphire with a scratch. The scale bar is 50 μm. (d) AFM image and (e) SEM image of monolayer MoS_2 film on sapphire. Scale bars are 2 μm. (f) SAED image and (g) HAADF-STEM image of MoS_2 film. Scale bars are 5 nm^{-1} and 5 nm, respectively. (h) Raman and (i) PL spectra of MoS_2 film on sapphire. (j) and (k) XPS spectra of MoS_2 film on sapphire.

monolayer MoS_2 continuous films on 2-in c-plane sapphire under the optimal conditions (0–1 mg NaCl, relatively adequate S/Mo ratio, and the addition of 0–1 sccm O_2 (with 300 sccm Ar); the detailed optimization process is shown below). The typical optical microscopy (OM) images (Fig. 1(c) and Fig. S1 in the Electronic Supplementary Material (ESM)) and the corresponding atomic force microscopy (AFM) images (Fig. 1(d) and Fig. S2 in the ESM) reveal that the obtained wafer is a continuous and monolayer film with high uniformity, little contamination, and no second layer visible. The scanning electron microscopy (SEM) image (Fig. 1(e)) reconfirms the smooth surface of the as-grown MoS_2 film on sapphire. The high-angle annular dark field scanning transmission electron microscopy (HAADF-STEM) was used to further investigate the crystallinity and quality of the as-grown monolayer MoS_2 film. Figure 1(f) shows the selected area electron diffraction (SAED) pattern of MoS_2 film, exhibiting only one set of hexagonal diffraction spots. The nearly perfect periodic atom arrangement of the honeycomb lattice of MoS_2 was observed (Fig. 1(g)), strongly suggesting the high-quality crystalline hexagonal structure of MoS_2 films.

Raman and photoluminescence (PL) spectra were further used to investigate the structure and optical properties of the as-grown MoS_2 film. Raman spectroscopy (Fig. 1(h)) of MoS_2/sapphire showed two obvious resonance peaks of E_{2g} and A_{1g} at 385 and 404 cm^{-1} with the peak distance (Δ) of 19 cm^{-1}, respectively, confirming the monolayer nature of the as-grown film [18, 45]. Raman mapping image of the synthesized MoS_2 film at A_{1g} mode (Fig. S3 in the ESM) shows rather uniform color contrast, suggesting a highly uniform crystal structure across the entire film. PL spectra of (Fig. 1(i)) the MoS_2 films show a single sharp excitonic A peak at ~ 660 nm with a narrow full width at half maxima (FWMH) of ~ 45 meV, suggesting the high crystalline quality. We further evaluated the chemical composition and elemental bonding configuration of MoS_2 films by X-ray photoelectron spectroscopy (XPS). In Fig. 1(j), two characteristic peaks arising from Mo $3d_{5/2}$ and Mo $3d_{3/2}$ orbitals located at 229.8 and 232.9 eV with ~ 3.1 eV spin-orbit splitting, respectively, corresponding to Mo^{4+} peaks of Mo–S bonds. The two peaks centered at 162.6 and 163.8 eV are assigned to the binding energy of S $2p_{3/2}$ and $2p_{1/2}$ of MoS_2, respectively (Fig. 1(k)). These binding energies are all consistent with the reported values for MoS_2 crystal [46–48].

2.2 Key factors affecting the synthesis of wafer-scale MoS_2 films

The synthesis of 2D materials is a non-equilibrium process involving multi-component, multi-parameter, and complex surface/interface interactions. Various growth parameters during the CVD process (e.g., precursor concentration and ratio, growth temperature, solid/gas additives-salt/oxygen, and surface structure of growth substrate) can be used to adjust the domain size, morphology, quality, uniformity, and film coverage of the target materials. These parameters synergistically affect the processes of interfacial reaction and mass diffusion, which are the key to growing wafer-scale monolayer MoS_2 films.

Due to the high melting point of transition metals and their corresponding metal oxides, the vapor pressure of the metal oxide precursors is low, and thus the nucleation density and growth rate are too low during the CVD process, which is unfavorable for synthesizing wafer-scale films. Adding salt assistants can greatly reduce the melting point of the metal oxide precursor, making higher precursor mass flux to participate in the nucleation and growth process. The molten salt-assisted CVD method has been universally adopted to realize the synthesis of various 2D transition metal dichalcogenides (TMDs) [49].

In the absence of salt, even if the evaporation temperature of MoO_3 is 750 °C, only a very small amount of thick and small-size MoS_2 particles is deposited, along with black and un-sulfurized MoO_3 particles (Fig. S4 in the ESM). Benefiting from the addition of NaCl salt, the evaporation temperature of MoO_3 was reduced to 530 °C, and obvious MoS_2 deposition with the largest domain size of ~ 20 μm can be realized (Fig. 2). However, the vapor rate of the low melting point oxychloride intermediate is too fast, which makes it difficult to control the vapor pressure of the Mo precursor and the uniformity of the target product. Therefore, it is important to carefully control the dosage of NaCl to promote the uniform supply of Mo source. Figure 2(a) shows the MoS_2 on the sapphire with 5 mg of NaCl. 5 mg of NaCl is too excessive for the monolayer growth and excessive NaCl leads to a large thickness gradient of MoS_2, in which the contrast of the deposited MoS_2 contrast varies from bright gray to yellowish brown to light yellow (Fig. 2(a)). It is dominated by thick grains (Fig. $2(a_1)$) and high-density multilayers MoS_2 (Figs. $2(a_2)$ and $2(a_3)$) and occasionally has a few single-layer MoS_2 film regions (Fig. $2(a_4)$). With the dosage of NaCl reduced to 2 mg, although the overall color contrast of MoS_2 thickness has decreased (Fig. 2(b)), high-density nucleus and multilayers of MoS_2 can also be observed with a very small size (Figs. $2(b_1)$–$2(b_4)$). Further decreasing the amount of NaCl to 1 mg, uniform monolayer MoS_2 films with domain sizes of ~ 20 μm were obtained and showed relatively homogeneous optical contrast (light yellow) (Fig. 2(c)), as confirmed by the low and high magnification OM images (Figs. $2(c_1)$–$2(c_4)$)). Meanwhile, Raman and PL spectra showed that a high dosage of NaCl decreased the quality of the film, with a red shift in PL and an increase in the FWMH and Δ between A_{1g} and E_{2g} (Figs. 2(d)–2(f)). Such quality degradation can be ascribed to that excess NaCl is deposited on the surface of monolayer MoS_2 as tiny particles, as confirmed by the AFM characterization (Fig. 2(g)) [50, 51]. The roughnesses of the synthesized sample are 0.15 (1 mg NaCl), 0.35 (2 mg NaCl), and 0.88 nm (5 mg NaCl), respectively. Furthermore, the mobility of these MoS_2 devices with channel length/width (L/W) of 2/12 μm decreased to ~ 8.6 $cm^2 \cdot V^{-1} \cdot s^{-1}$ and the current density decreased to ~ 16.7 $\mu A \cdot \mu m^{-1}$ as the NaCl dosage increased from 1 to 5 mg (Fig. S5). Therefore, it is necessary to strictly control the amount of NaCl to ensure the slow and stable evaporation of MoO_3, and the uniform and high-quality growth of MoS_2 film.

The ratio of metal source to sulfur directly affects the shape, size, and quality of the grown TMD materials. According to the crystal growth principle, the shape of the monolayer MoS_2 is determined by the growth rate of the different edges [52, 53], in which the most energetically stable edges are the Mo zigzag (Mo-ZZ) edge and the S zigzag (S-ZZ) edge. In the Mo-sufficient atmosphere, Mo atoms preferentially react with the S-ZZ edge, which ultimately results in triangular MoS_2 domains with three Mo-ZZ edges, while the Mo:S corresponds to the stoichiometric ratio of MoS_2, which results in hexagonal MoS_2 domains. The S-rich atmosphere is similar to the Mo-sufficient atmosphere, and eventually, a triangular MoS_2 domain formed by three S-ZZ edges is obtained [54]. Generally, the ratio of precursor Mo to S in the vapor phase can be controlled by the temperature of MoO_3 and S powder, the relative position of the growth substrate to the Mo source, and the carrier gas flow rate [55–58].

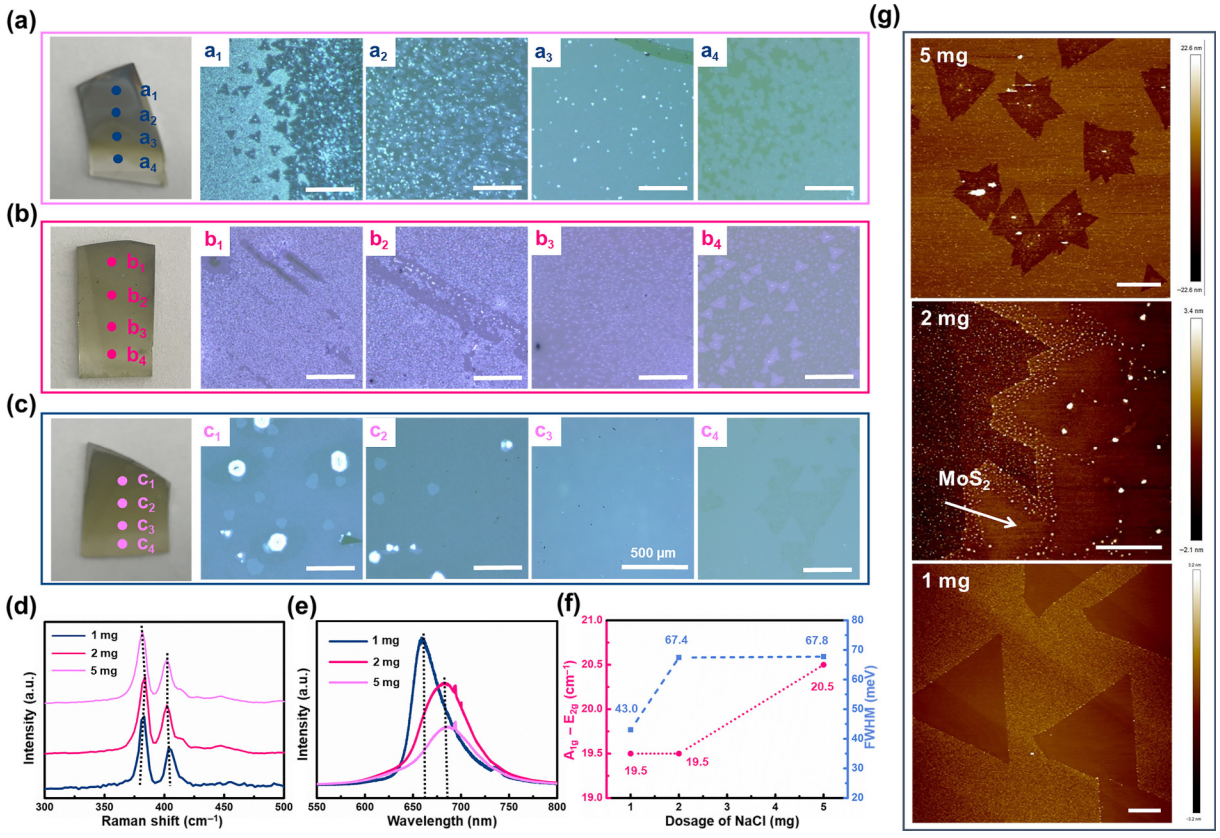

Figure 2 Effect of salt additive NaCl dosage on the growth of monolayer MoS_2. (a)–(c) Photographs and corresponding OM images of MoS_2 grown at different positions on sapphire by using different NaCl dosages of 5, 2, and 1 mg (with 50 mg MoO_3 precursors), respectively. Scale bars are 20 μm. (d) Raman and (e) PL spectra of MoS_2 by using different NaCl dosages. (f) The corresponding statistic Δ (the distance between A_{1g} and E_{2g}) value and PL FHWM of monolayer MoS_2. (g) AFM images of MoS_2 were obtained when NaCl dosage was 1 (bottom panel), 2 (central panel), and 5 mg (top panel), respectively. Scale bars are 5 μm.

The concentration gradient of the S vapor, when it reaches the substrate, is negligible due to the long distance between them. On the contrary, Mo precursor vapor arrives at the substrate surface with a very pronounced concentration gradient. Therefore, the concentration of Mo precursor and the distance between Mo source and sapphire (d) determine the Mo/S ratio. In our experiment, the temperature of S powder was fixed at 220 °C to ensure sufficient supply, the addition of NaCl was 1 mg, and the effect of the heating temperature of MoO_3 on the growth of MoS_2 was investigated. As shown in Fig. 3(a), the excessive of MoO_3 led to incomplete sulfidation (white streaks of molybdenum oxide intermediates Mo_xO_{3-x}, Fig. S6(a) in the ESM) when the evaporation temperature of MoO_3 was 600 °C (the distance between the MoO_3 precursor and substrate was 20 cm). As the evaporation temperature of MoO_3 dropped to 580 °C, MoO_3 was fully sulfurized and the S/Mo ratio was slightly higher than the stoichiometric ratio of 2/1, producing triangular and truncated triangular MoS_2 domains with smooth edges (Fig. 3(b)). When the evaporation temperature of MoO_3 was further reduced to 530 °C (S/Mo ratio > 2/1), regular triangular MoS_2 domains were deposited on the sapphire and further stitched to form a continuous film (Fig. 3(c)). The high-density triangle MoS_2 domains are conducive to the formation of high-quality MoS_2 continuous films (Figs. 3(c) and 3(d)).

Another experimental variable controlling the precursor Mo to S ratio in the vapor phase is the distance between the MoO_3 and sapphire substrate. When $d \leq 14$ cm (with the temperature of MoO_3 to be 530 °C), black particles of bulk phase MoS_2 and strips of molybdenum oxides with incomplete reaction were deposited on the sapphire substrate (Fig. 3(e) and Fig. S6(b) in the ESM). In this case, the mixing of gaseous Mo precursor and S is not sufficient and precursor atoms are unable to migrate to the exact site in time due to the concentration of both MoO_3 and S powder being too high. As d increased to 20 cm, regular triangular MoS_2 nanosheets with a high nucleation density (~ 2.67×10^6 cm^{-2}) and an average size of 5 μm were formed (Figs. 3(f) and 3(h)). In this case, a sufficient and stable supply of MoO_3 and S sources can guarantee the complete reaction, and thus continuous monolayer MoS_2 film can be obtained by further increasing the reaction time (the inset in Fig. 3(f)). When the distance was further increased to 25 cm, the concentration of Mo source reaching the substrate was significantly reduced, resulting in low nucleation density (~ 1.02×10^5 cm^{-2}) and triangular MoS_2 domains with large size (10 μm) and rough S-ZZ edges (Figs. 3(g) and 3(h)) [54, 59], which is not conducive to the stitching of single MoS_2 domains into continuous films. The schematics of Fig. 3(i) summarize the size and shape evolution process of the MoS_2 monolayer as the ratio of Mo to S changes. Therefore, it is necessary to adjust the appropriate growth position during the growth of wafer-scale MoS_2 films and the optimization distance in this experiment is 16–23 cm.

The evaporation temperature of MoO_3 and the distance between MOO_3 and the substrate directly affect the precursor Mo to S ratio in the vapor phase, which influences the shape and size of the grown MoS_2. High Mo:S led to incomplete sulfidation and deposition of by-products while low Mo:S hindered the stitching of single MoS_2 domains into continuous films. In a word, adequate

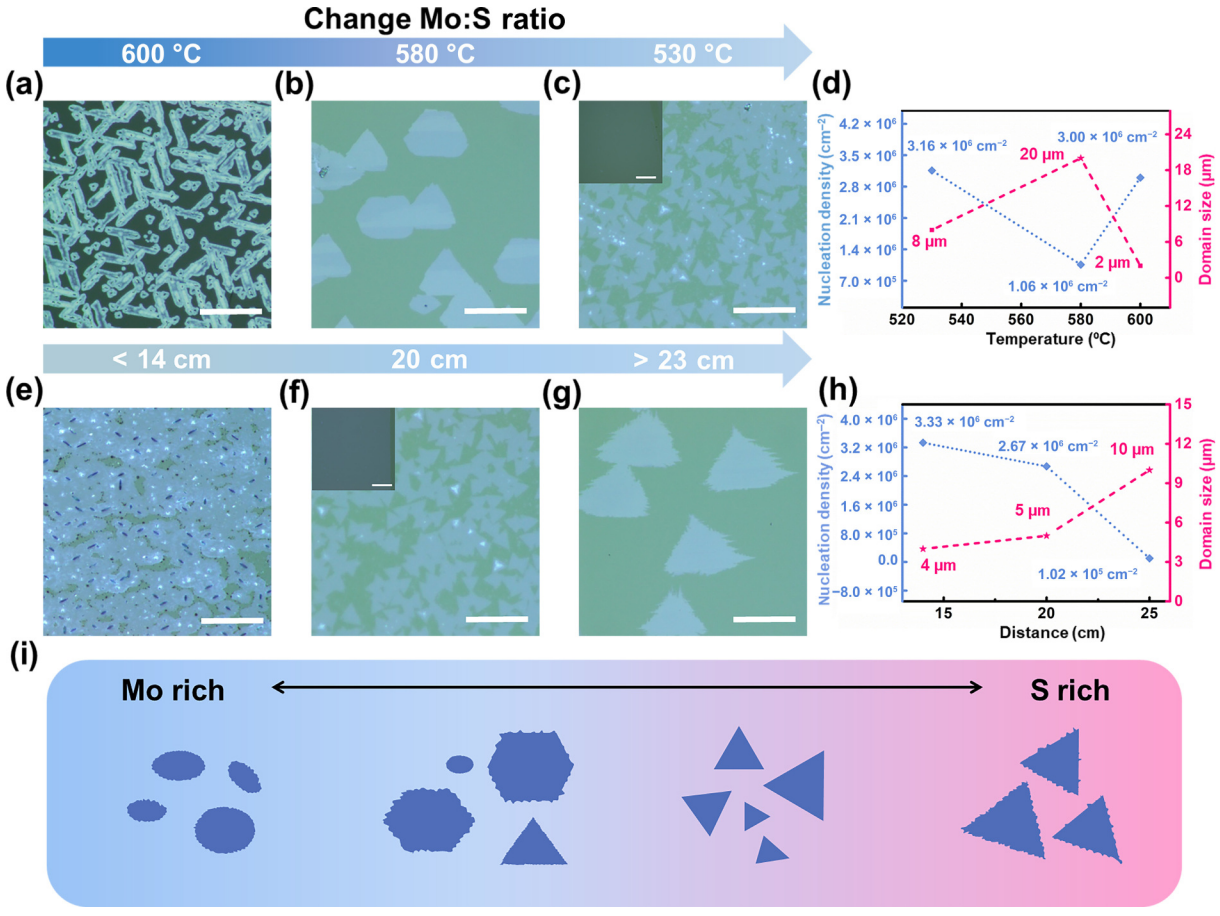

Figure 3 Effect of Mo:S ratio in vapor phase on MoS_2 growth. (a)–(c) Morphological changes of MoS_2 under different heating temperatures of MoO_3 with fixed distance between MoO_3 and the substrate of 20 cm and 1 mg NaCl, including (a) white striped intermediates, (b) smooth triangles and truncated triangles, and (c) regular triangles of MoS_2 at MoO_3 temperatures of (a) 600 °C, (b) 580 °C, and (c) 530 °C, respectively. Scale bars are 20 μm. The inset in (c) shows the corresponding continuous MoS_2 films at the corresponding growth conditions. (d) Extracted nucleation density and average domain size of MoS_2 under different MoO_3 evaporation temperatures. (e)–(g) Morphological changes of MoS_2 under different distances between the MoO_3 precursor and the substrate (*d*) with fixed MoO_3 precursor temperature of 530 °C, including (e) d = 14 cm, (f) d = 20 cm, and (g) d = 23 cm. The inset in (f) shows the corresponding continuous MoS_2 films at the corresponding growth conditions. Scale bars are 20 μm. (h) Nucleation density and average domain size of MoS_2 concerning *d*. (i) Schematic illustration of the size and shape evolution of MoS_2 monolayer by changing the ratio of precursor Mo to S in the vapor phase.

Mo:S was essential for the synthesis of MoS_2 films with regularly shaped domains.

A small amount of O_2 can inhibit the nucleation density of MoS_2 by etching effect and promote the large-size epitaxy of individual domains, thereby reducing the grain boundary density and improving the electrical quality of wafer-scale MoS_2 films. Meanwhile, the electrical properties of MoS_2 are enhanced, including the increase of field effect mobility and conductivity due to the doping of O_2 that reduces the band gap of MoS_2 [18, 26, 60–62]. On the other hand, a small amount of O_2 can prevent the sulfation poisoning of MoO_3 and provide a stable feedstock of the molybdenum source.

In the absence of O_2, the high MoS_2 nucleation density leads to small sizes of individual domains, irregular shapes with an average size of ~ 2 μm, and high film grain boundary density (Figs. 4(a) and 4(e)). When the O_2 flow rate reached 1 sccm, regular triangular MoS_2 was deposited with the domain size increasing to ~ 10 μm, the nucleation density of MoS_2 decreased to ~ 3.16×10^6 cm^{-2}, and the uniform film was synthesized (Fig. 4(b)). However, when the O_2 flow rates were varied from 2 to 5 sccm (Figs. 4(c) and 4(d)), the etching effect of O_2 on MoS_2 can be observed and the etching rate of O_2 was much larger than the growth rate of MoS_2, and the small number of MoS_2 nucleation dots (bright white areas) were deposited on the sapphire (Fig. 4(d)). Figure 4(e) demonstrates the variation of nucleation density and average domain size of MoS_2 with the O_2 flow rate and an appropriate nucleation density and the maximum domain size was observed at 1 sccm O_2. The presence of O_2 at high temperature, on the other hand, also causes etching of MoS_2. O_2 flow rate needs to be carefully controlled for the balance between etching and growth of MoS_2. The nucleation density is controlled with 3 sccm of O_2 during the nucleation stage, while the O_2 flow is reduced to 1 sccm during the growth stage (Fig. 4(f)). During the growth process, the sapphire substrate, which had been pre-annealed in air at 1000 °C for 4 h, was annealed again in Ar atmosphere at 930 °C for 30 min. Figure 4(g) illustrates the timeline profiles of temperature at S, MoO_3, and substrate locations. In the regulation of wafer-level MoS_2 film growth, a balance between the growth rate and etching rate needs to be maintained.

The control of the unidirectional growth of MoS_2 domains is essential for synthesizing high-quality MoS_2 films, which is generally achieved through the interaction between the material and the substrate or through the induction of steps on the substrate surface. The orientation of MoS_2 was random on untreated sapphire (Fig. 5(a)). The growth of MoS_2 with certain orientations

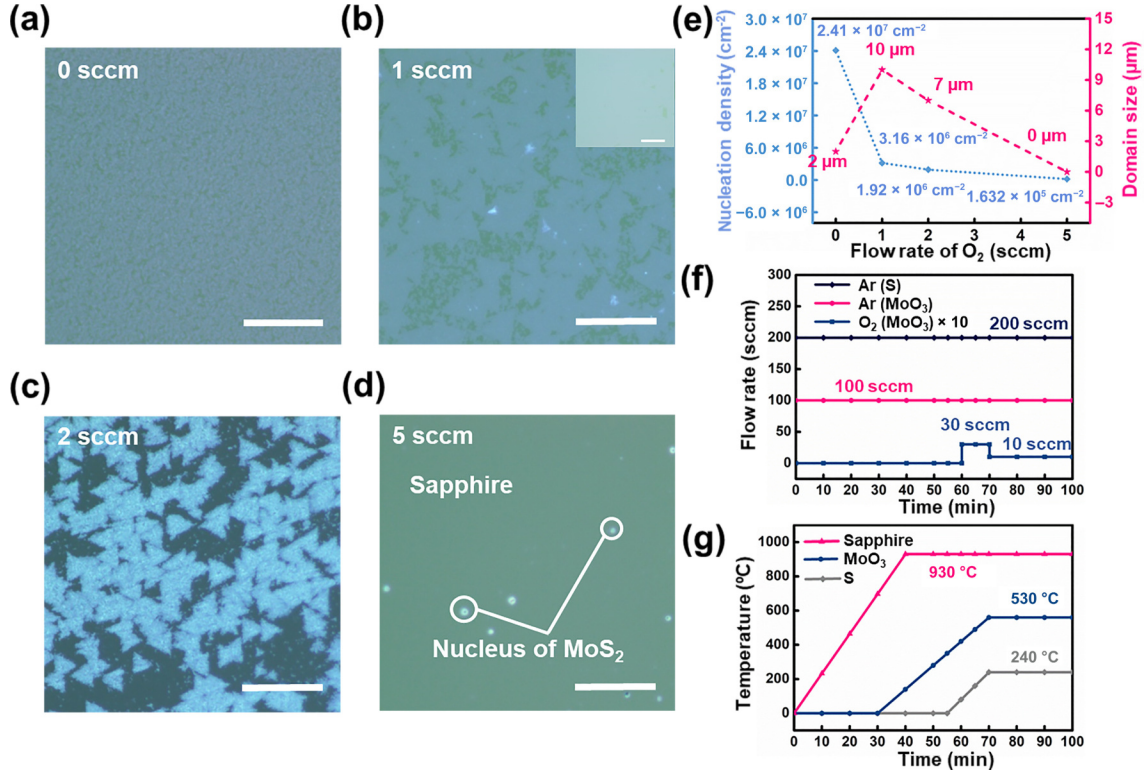

Figure 4 Effect of the O_2 dosage on the growth of MoS_2. (a)–(d) OM images of MoS_2 at 0, 1, 2, and 5 sccm O_2, respectively. Scale bars are 20 μm. The inset in (b) shows the corresponding continuous MoS_2 films at corresponding growth conditions. (e) The change of nucleation density and average domain size of MoS_2 under different O_2 flow rates. (f) and (g) Timeline profiles of gas flow rate and temperature at S, MoO_3, and substrate locations, respectively.

(~ 36% 0°-oriented and ~ 15% 60°-oriented) was induced by the formation of a regular step structure on the sapphire surface after the high-temperature annealing treatment in air at 1000 °C for 4 h (Fig. 5(b)). Interestingly, antiparallel oriented MoS_2 domains (~ 60% 0°-oriented and ~ 36% 60°-oriented) and continued MoS_2 films were obtained when the sapphire substrate was annealed again at the growth temperature for 30 min before the feedstock was passed for growth during the CVD process (Fig. 5(c)).

The growth substrate determines the properties of MoS_2 such as morphology, size, and orientation. The growth of MoS_2 on m-plane sapphire (~ 40% 0°-oriented and ~ 50% 60°-oriented) was similar to that of c-plane sapphire, with the difference that the MoS_2 was a triangle or hexagon with rounded edges (Fig. 5(d)). The morphology of MoS_2 shifts to truncated triangles with unidirectional domains (Fig. 5(e)), which is a powerful option for the growth of wafer-scale single-crystalline 2D TMDs thin film, when annealed a-plane sapphire is used as substrate. The reason for this difference may lie in the symmetry of the MoS_2 and the substrate and step orientation of sapphire (Fig. S7 in the ESM). c-plane sapphire has 3-fold symmetry, and the atoms of the top layer of the substrate generally have a higher symmetry (6-fold symmetry). So, there are generally two anti-parallel MoS_2 islands on c-plane sapphire with steps along <11$\bar{2}$0> orientation while parallel aligned MoS_2 islands could be realized on a-plane sapphire with twofold symmetry with steps along <1$\bar{1}$01> orientation by precise control of the experimental condition [42, 43].

2.3 Devices made from as-synthesized MoS_2 films

The high quality of the as-grown monolayer MoS_2, in principle, would enable the superior device performances [38]. To characterize the electronic quality of the monolayer MoS_2 films synthesized at optimized growth parameters, we transferred these films onto the 90 nm Si_3N_4 substrates for FETs device fabrication. The output and transfer curves of a typical MoS_2 device with channel length/width (L/W) of 2/12 μm are shown in Figs. 6(a) and 6(b), respectively. The drain current–voltage (I_{ds}–V_{ds}) output curves exhibit linear characteristics at low bias, suggesting satisfactory contact formation (Fig. 6(a)). The transfer characteristics also show clear current saturation with the highest on-current value of up to 89.2 μA·μm^{-1} (Fig. 6(b)). The subthreshold swing (SS) is about 1019 mV·dec^{-1}. We measured 20 randomly picked devices in the batch, and the statistical data are shown in Figs. 6(c)–6(f). We can see that the average saturated current density of these devices is 56.3 μA·μm^{-1}, and the average and best mobilities are 28.5 and 45.0 cm^2·V^{-1}·s^{-1}, respectively (Figs. 6(e) and 6(f)), suggesting high electronic uniformity of the MoS_2 films. In fact, there are many factors affecting device performance, including but not limited to the film itself, as well as the overall structural design including the electrical contact interface and the gate dielectric [63, 64]. It has a very broad prospect in improving the performance of two-dimensional semiconductor devices and promoting the large-scale integration of two-dimensional semiconductor devices.

3 Conclusions

In summary, we reveal the influence of critical growth parameters on the synthesis of wafer-scale MoS_2 films and successfully prepared 2-in monolayer MoS_2 continuous films on c-plane sapphire under optimized growth conditions (0–1 mg NaCl, adequate S/Mo ratio, and 0–1 sccm O_2). The dosage of NaCl has important influences on the quality and film coverage of MoS_2, and the S/Mo ratio affects the shape and size of the grown MoS_2, while

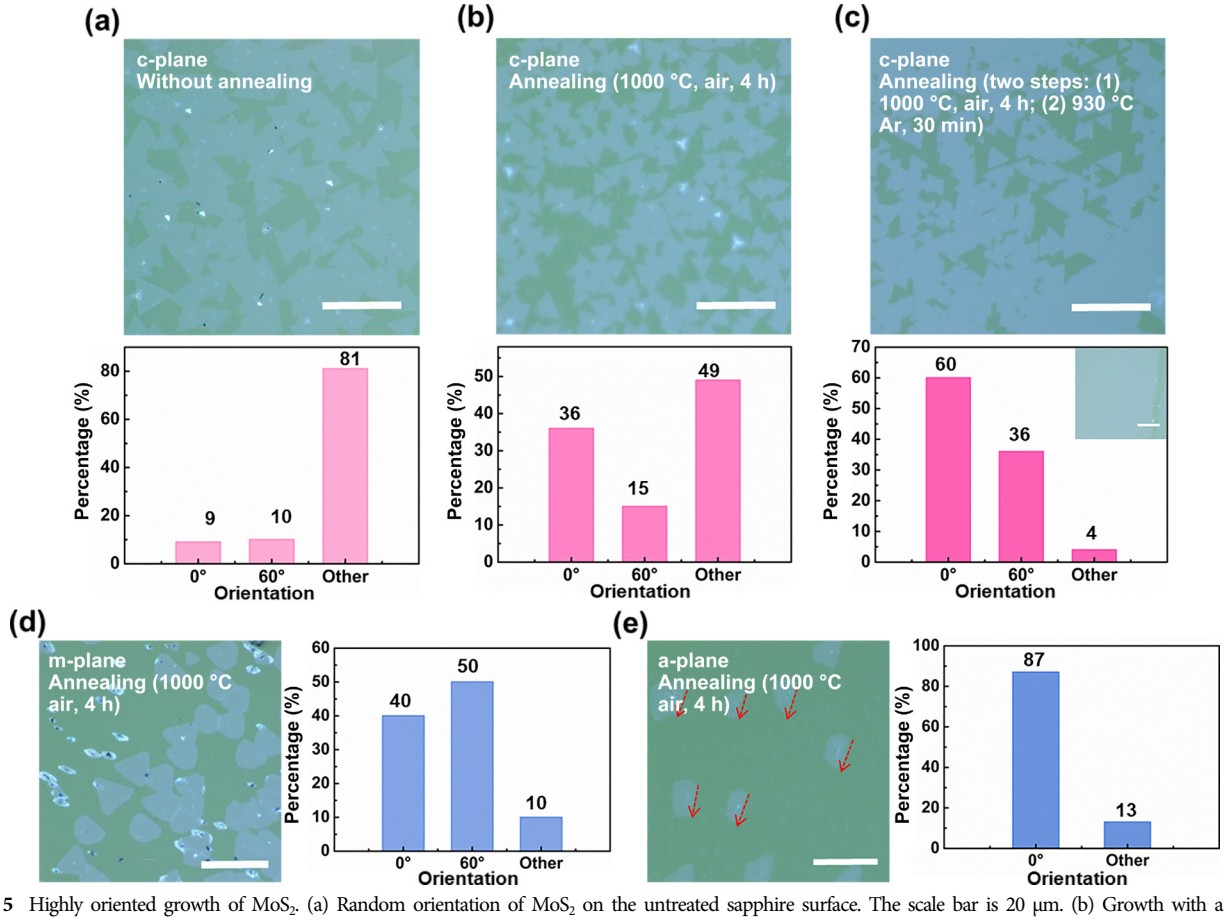

Figure 5 Highly oriented growth of MoS_2. (a) Random orientation of MoS_2 on the untreated sapphire surface. The scale bar is 20 μm. (b) Growth with a certain orientation MoS_2 was induced by the formation of a regular step structure on the sapphire surface after the high-temperature annealing treatment in air at 1000 °C for 4 h. The scale bar is 20 μm. (c) MoS_2 domains with antiparallel orientation on the step surface of sapphire after two steps annealing. The inset shows the corresponding continuous MoS_2 films at corresponding growth conditions. The scale bar is 20 μm. (d) and (e) Growth of oriented MoS_2 on m- and a-plane sapphire after annealing at 1000 °C for 4 h, respectively. Scale bars are 20 μm.

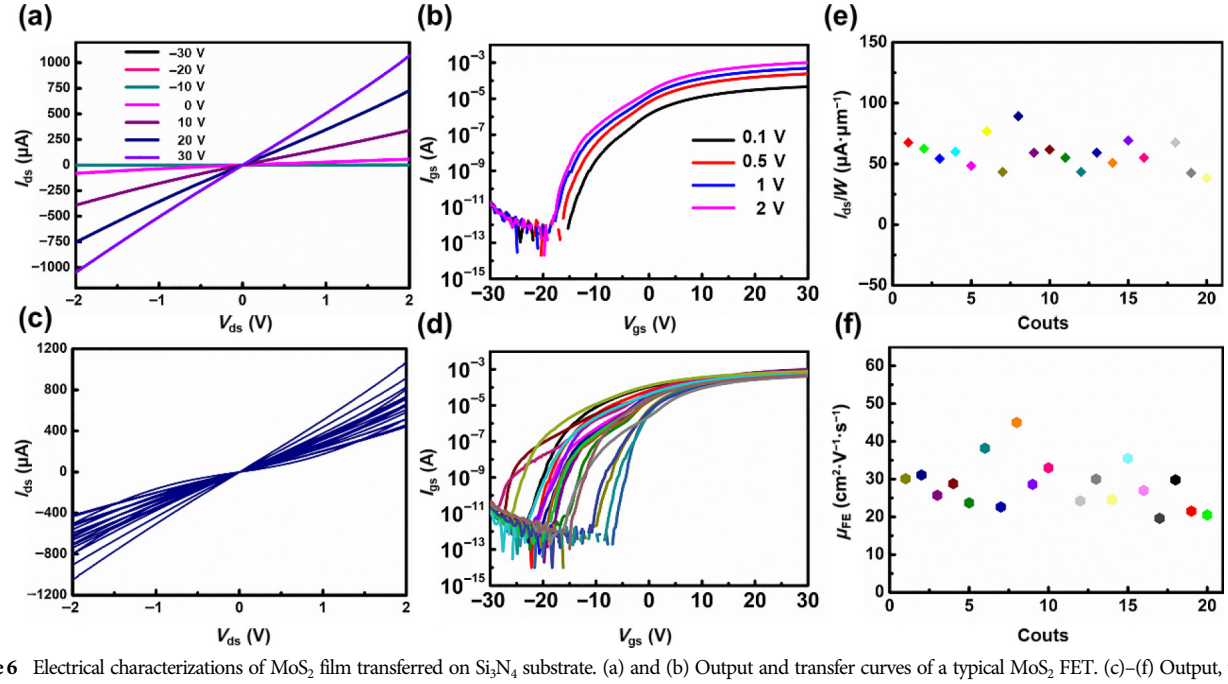

Figure 6 Electrical characterizations of MoS_2 film transferred on Si_3N_4 substrate. (a) and (b) Output and transfer curves of a typical MoS_2 FET. (c)–(f) Output, transfer curves, saturation current, and field-effect mobility from 20 devices, respectively; the device fabricated at random positions of a wafer sample.

the flow rate of O_2 plays a key role in controlling the nucleation density and domain size. We further discovered that a-plane sapphire can easily guide the unidirectional growth of MoS_2 compared with c-plane and m-plane sapphire. As-grown films are uniform and high quality, which was demonstrated by microscopies, spectroscopies, and electrical measurements. The FETs made from the as-synthesized monolayer MoS_2 film under optimized growth parameters show the average and best mobilities of 28.5 and 45 $cm^2 \cdot V^{-1} \cdot s^{-1}$, respectively. This study revealed the influence of key growth parameters and provided systematic support for the synthesis of wafer-scale MoS_2 on c-plane sapphire.

4 Methods

4.1 CVD growth of wafer-scale MoS_2 on sapphire

The MoS_2 film growth on sapphire was performed in a low-pressure three-temperature-zone CVD system. S powders (99.5%, Shanghai Aladdin Biochemical Technology) were placed at the upstream end of a quartz tube heated independently with an extra heating band and carried by 200 sccm Ar. MoO_3 powders (99.5%, Shanghai Aladdin Biochemical Technology) and NaCl (95%, Shanghai Aladdin Biochemical Technology) were carried by 100 sccm Ar into the growth chamber separately from the S vapor. During the growth process, the temperatures for the S source, MoO_3 source, and substrate were 240, 530, and 930 °C, respectively. For a typical growth, the growth duration was ~ 30 min and the pressure in the growth chamber was kept at ~ 100 Pa.

4.2 Materials characterization

The as-synthesized monolayer MoS_2 film was characterized by an optical microscope (DP27, OLYMPUS), The structure and thickness of as-grown monolayer MoS_2 film were characterized by XPS (charging referenced to the C 1s peak at 284.8 eV) and atomic force microscopy (Bioscope system BRUCKER), respectively. The Raman and PL spectra/maps were obtained by a confocal microscope (inVia Reflex, Renishaw with 532 nm laser as the excitation source). A HAADF-STEM image was collected and determined by scanning transmission electron microscopy (Thermo Scientific, Themis Z).

4.3 Transfer of MoS_2 film

First, polymethyl methacrylate (PMMA) was spin-coated on MoS_2/sapphire twice at a speed of 4000 r.p.m. and then baked at 120 °C for 2.5 min. Next, the blue tape with a small rectangular hole was attached to the sample, and then this sample was immersed in a water solution for 2 h. The blue tape/PMMA/MoS_2 layer was peeled off using tweezers and moved to the surface of pure water for washing several times before this layer was transferred to the target substrate and the PMMA/MoS_2 layer was released on the substrate. After full release, the sample was washed in acetone for 30 min to remove all polymer.

4.4 Device fabrication and characterization

For the vdW integration devices, the metal electrodes were defined onto a sacrificial substrate (285-nm-thick SiO_2/Si) following hexamethyldisilazane treatment (80 °C in an oven for 10–20 min) before the prefabricated source and drain electrodes were transferred to the MoS_2 film by the vdW integration approach. After the vacuum metallization process, photolithography or electron-beam lithography was used to define the channel regions, and then a redundant MoS_2 film was etched by oxygen plasma. The metal–semiconductor interface was kept clean because the polymer residue of the MoS_2 surface was usually very hard and could be removed after the plasma etching process. All device transport measurements were conducted in a Lakeshore vacuum probe station with semiconductor parameter analyzers (Keysight 2912A and Agilent B1500).

Electronic Supplementary Material: Supplementary material (OM images, AFM images, Raman mapping images, and Raman spectroscopy measurements) is available in the online version of this article at https://doi.org/10.26599/NR.2025.94907140.

Data availability

All data needed to support the conclusions in the paper are presented in the manuscript and the Electronic Supplementary Material. Additional data related to this paper may be requested from the corresponding author upon request.

Acknowledgements

This work was granted by the National Key Research and Development Program of the of China (No. 2022YFA1203801), the National Natural Science Foundation of China (Nos. 51991340, 51991343, 52221001, 52102168, and 52372145), Hunan Key Research and Development Program Project (No. 2022GK2005), the Natural Science Foundation of Hunan Province (No. 2023JJ20009), the Hunan Province "Huxiang Talents" Project (No. 2023RC3092), the Natural Science Foundation of Chongqing, China (No. cstc2021jcyj-msxmX0321), and the Doctoral Scientific Research Foundation of Hubei University of Automotive Technology (No. BK202486).

Declaration of competing interest

All the contributing authors reports no conflict of interests in this work.

Author contribution statement

R. S.: Data curation, validation, writing manuscript, experimental design. D. Y. S.: Data curation, validation. D. Y. L.: Data curation. J. Y. L.: Data curation. Z. M. Z.: Data curation. J. M. T.: Data curation. L. C.: Data curation. B. L.: Data curation. J. L.: funding acquisition. writing manuscript. X. D. D: Project administration, funding acquisition, experimental design. All the authors have approved the final manuscript.

Use of AI statement

None.

References

[1] Desai, S. B.; Madhvapathy, S. R.; Sachid, A. B.; Llinas, J. P.; Wang, Q. X.; Ahn, G. H.; Pitner, G.; Kim, M. J.; Bokor, J.; Hu, C. M. et al. MoS_2 transistors with 1-nanometer gate lengths. *Science* **2016**, *354*, 99–102.

[2] Chen, M. L.; Sun, X. D.; Liu, H.; Wang, H. W.; Zhu, Q. B.; Wang, S.

S.; Du, H. F.; Dong, B. J.; Zhang, J.; Sun, Y. et al. A FinFET with one atomic layer channel. *Nat. Commun.* **2020**, *11*, 1205.

[3] Feng, J. D.; Graf, M.; Liu, K.; Ovchinnikov, D.; Dumcenco, D.; Heiranian, M.; Nandigana, V.; Aluru, N. R.; Kis, A.; Radenovic, A. Single-layer MoS_2 nanopores as nanopower generators. *Nature* **2016**, *536*, 197–200.

[4] Zhao, J.; Chen, W.; Meng, J. L.; Yu, H.; Liao, M. Z.; Zhu, J. Q.; Yang, R.; Shi, D. X.; Zhang, G. Y. Integrated flexible and high-quality thin film transistors based on monolayer MoS_2. *Adv. Electron. Mater.* **2016**, *2*, 1500379.

[5] Tao, L.; Chen, K.; Chen, Z. F.; Chen, W. J.; Gui, X. C.; Chen, H. J.; Li, X. M.; Xu, J. B. Centimeter-scale CVD growth of highly crystalline single-layer MoS_2 film with spatial homogeneity and the visualization of grain boundaries. *ACS Appl. Mater. Interfaces* **2017**, *9*, 12073–12081.

[6] Zhou, S. X.; Jiao, L. Y. Growth of single-crystalline transition metal dichalcogenides monolayers with large-size. *Chem. Res. Chin. Univ.* **2020**, *36*, 511–517.

[7] Chang, M. C.; Ho, P. H.; Tseng, M. F.; Lin, F. Y.; Hou, C. H.; Lin, I. K.; Wang, H.; Huang, P. P.; Chiang, C. H.; Yang, Y. C. et al. Fast growth of large-grain and continuous MoS_2 films through a self-capping vapor–liquid–solid method. *Nat. Commun.* **2020**, *11*, 3682.

[8] Wu, F.; Tian, H.; Shen, Y.; Hou, Z.; Ren, J.; Gou, G. Y.; Sun, Y. B.; Yang, Y.; Ren, T. L. Vertical MoS_2 transistors with sub-1-nm gate lengths. *Nature* **2022**, *603*, 259–264.

[9] Liu, L. T.; Kong, L. G.; Li, Q. Y.; He, C. L.; Ren, L. W.; Tao, Q. Y.; Yang, X. D.; Lin, J.; Zhao, B.; Li, Z. W. et al. Transferred van der Waals metal electrodes for sub-1-nm MoS_2 vertical transistors. *Nat. Electron.* **2021**, *4*, 342–347.

[10] He, Z. G.; Guan, H. Y.; Liang, X. J.; Chen, J. T.; Xie, M. Y.; Luo, K. W.; An, R.; Ma, L.; Ma, F. K.; Yang, T. F. et al. Broadband, polarization-sensitive, and self-powered high-performance photodetection of hetero-integrated MoS_2 on lithium niobate. *Research* **2023**, *6*, 0199.

[11] Tan, C.; Wu, H. J.; Zhao, M. M.; Jili, X. B.; Yang, L.; Gao, L. B.; Wang, Z. G. Gate-switchable BST ferroelectric MoS_2 FETs for non-volatile digital memory and analog memristor. *Adv. Funct. Mater.* **2024**, *34*, 2405293.

[12] Domke, K. F. Monitoring catalytic nanosites in action. *Nat. Catal.* **2024**, *7*, 613–614.

[13] Lu, Y. C.; Huang, J. K.; Chao, K. Y.; Li, L. J.; Hu, V. P. H. Projected performance of Si- and 2D-material-based SRAM circuits ranging from 16 nm to 1 nm technology nodes. *Nat. Nanotechnol.* **2024**, *19*, 1066–1072.

[14] Parker, M. 3D integration proceeds tier-by-tier. *Nat. Electron.* **2024**, *7*, 429.

[15] Cui, M. Y.; Qian, L. L.; Lu, K.; Liu, J. J.; Chu, B. B.; Wu, X. F.; Dong, F. L.; Song, B.; He, Y. Defect-rich metastable MoS_2 promotes macrophage reprogramming in breast cancer: A clinical perspective. *Small* **2024**, *20*, 2402101.

[16] Zuo, Y. G.; Liu, C.; Ding, L. P.; Qiao, R. X.; Tian, J. P.; Liu, C.; Wang, Q. H.; Xue, G. D.; You, Y. L.; Guo, Q. L. et al. Robust growth of two-dimensional metal dichalcogenides and their alloys by active chalcogen monomer supply. *Nat. Commun.* **2022**, *13*, 1007.

[17] Wang, Q. Q.; Tang, J.; Li, X. M.; Tian, J. P.; Liang, J.; Li, N.; Ji, D. P.; Xian, L. D.; Guo, Y. T.; Li, L. et al. Layer-by-layer epitaxy of multi-layer MoS_2 wafers. *Natl. Sci. Rev.* **2022**, *9*, nwac077.

[18] Yu, H.; Liao, M. Z.; Zhao, W. J.; Liu, G. D.; Zhou, X. J.; Wei, Z.; Xu, X. X.; Liu, K. H.; Hu, Z. H.; Deng, K. et al. Wafer-scale growth and transfer of highly-oriented monolayer MoS_2 continuous films. *ACS Nano* **2017**, *11*, 12001–12007.

[19] Yu, H.; Huang, L. F.; Zhou, L. Y.; Peng, Y. L.; Li, X. Z.; Yin, P.; Zhao, J. J.; Zhu, M. T.; Wang, S. P.; Liu, J. Y. et al. Eight in. wafer-scale epitaxial monolayer MoS_2. *Adv. Mater.* **2024**, *36*, 2402855.

[20] Kalanyan, B.; Kimes, W. A.; Beams, R.; Stranick, S. J.; Garratt, E.; Kalish, I.; Davydov, A. V.; Kanjolia, R. K.; Maslar, J. E. Rapid wafer-scale growth of polycrystalline 2H-MoS_2 by pulsed metal-organic chemical vapor deposition. *Chem. Mater.* **2017**, *29*, 6279–6288.

[21] Seol, M.; Lee, M. H.; Kim, H.; Shin, K. W.; Cho, Y.; Jeon, I.; Jeong, M.; Lee, H. I.; Park, J.; Shin, H. J. High-throughput growth of wafer-scale monolayer transition metal dichalcogenide via vertical ostwald ripening. *Adv. Mater.* **2020**, *32*, 2003542.

[22] Kim, H.; Ovchinnikov, D.; Deiana, D.; Unuchek, D.; Kis, A. Suppressing nucleation in metal-organic chemical vapor deposition of MoS_2 monolayers by alkali metal halides. *Nano Lett.* **2017**, *17*, 5056–5063.

[23] Liu, L.; Huang, Y. Z.; Sha, J. J.; Chen, Y. F. Layer-controlled precise fabrication of ultrathin MoS_2 films by atomic layer deposition. *Nanotechnology* **2017**, *28*, 195605.

[24] Jurca, T.; Moody, M. J.; Henning, A.; Emery, J. D.; Wang, B. H.; Tan, J. M.; Lohr, T. L.; Lauhon, L. J.; Marks, T. J. Low-temperature atomic layer deposition of MoS_2 films. *Angew. Chem., Int. Ed.* **2017**, *56*, 4991–4995.

[25] Liu, H.; Chen, L.; Zhu, H.; Sun, Q. Q.; Ding, S. J.; Zhou, P.; Zhang, D. W. Atomic layer deposited 2D MoS_2 atomic crystals: From material to circuit. *Nano Res.* **2020**, *13*, 1644–1650.

[26] Wang, Q. Q.; Li, N.; Tang, J.; Zhu, J. Q.; Zhang, Q. H.; Jia, Q.; Lu, Y.; Wei, Z.; Yu, H.; Zhao, Y. C. et al. Wafer-scale highly oriented monolayer MoS_2 with large domain sizes. *Nano Lett.* **2020**, *20*, 7193–7199.

[27] Kim, K. S.; Lee, D.; Chang, C. S.; Seo, S.; Hu, Y. Q.; Cha, S.; Kim, H.; Shin, J.; Lee, J. H.; Lee, S. et al. Non-epitaxial single-crystal 2D material growth by geometric confinement. *Nature* **2023**, *614*, 88–94.

[28] Xia, Y.; Chen, X. Y.; Wei, J. C.; Wang, S. Y.; Chen, S. Y.; Wu, S. M.; Ji, M. B.; Sun, Z. Z.; Xu, Z. H.; Bao, W. Z. et al. 12-inch growth of uniform MoS_2 monolayer for integrated circuit manufacture. *Nat. Mater.* **2023**, *22*, 1324–1331.

[29] Zhu, J. D.; Park, J. H.; Vitale, S. A.; Ge, W. J.; Jung, G. S.; Wang, J. T.; Mohamed, M.; Zhang, T. Y.; Ashok, M.; Xue, M. T. et al. Low-thermal-budget synthesis of monolayer molybdenum disulfide for silicon back-end-of-line integration on a 200 mm platform. *Nat. Nanotechnol.* **2023**, *18*, 456–463.

[30] Yang, P. F.; Zou, X. L.; Zhang, Z. P.; Hong, M.; Shi, J. P.; Chen, S. L.; Shu, J. P.; Zhao, L. Y.; Jiang, S. L.; Zhou, X. B. et al. Batch production of 6-inch uniform monolayer molybdenum disulfide catalyzed by sodium in glass. *Nat. Commun.* **2018**, *9*, 979.

[31] Zhu, H. Y.; Nayir, N.; Choudhury, T. H.; Bansal, A.; Huet, B.; Zhang, K. Y.; Puretzky, A. A.; Bachu, S.; York, K.; Mc Knight, T. V. et al. Step engineering for nucleation and domain orientation control in WSe_2 epitaxy on c-plane sapphire. *Nat. Nanotechnol.* **2023**, *18*, 1295–1302.

[32] Chubarov, M.; Choudhury, T. H.; Hickey, D. R.; Bachu, S.; Zhang, T. Y.; Sebastian, A.; Bansal, A.; Zhu, H.; Y. Trainor, N. ; Das, S. et al. Wafer-scale epitaxial growth of unidirectional WS_2 monolayers on sapphire. *ACS Nano* **2021**, *15*, 2532–2541.

[33] Chiappe, D.; Ludwig, J.; Leonhardt, A.; El Kazzi, S.; Nalin Mehta, A.; Nuytten, T.; Celano, U.; Sutar, S.; Pourtois, G.; Caymax, M. et al. Layer-controlled epitaxy of 2D semiconductors: Bridging nanoscale phenomena to wafer-scale uniformity. *Nanotechnology* **2018**, *29*, 425602.

[34] Zhu, J. T.; Xu, H.; Zou, G. F.; Zhang, W.; Chai, R. Q.; Choi, J.; Wu, J.; Liu, H. Y.; Shen, G. Z.; Fan, H. Y. MoS_2-OH bilayer-mediated growth of inch-sized monolayer MoS_2 on arbitrary substrates. *J. Am. Chem. Soc.* **2019**, *141*, 5392–5401.

[35] Yang, P. F.; Liu, F. C.; Li, X.; Hu, J. Y.; Zhou, F.; Zhu, L. J.; Chen, Q.; Gao, P.; Zhang, Y. F. Highly reproducible epitaxial growth of wafer-scale single-crystal monolayer MoS_2 on sapphire. *Small Methods* **2023**, *7*, 2300165.

[36] Cun, H. Y.; Macha, M.; Kim, H.; Liu, K.; Zhao, Y. F.; LaGrange, T.; Kis, A.; Radenovic, A. Wafer-scale MOCVD growth of monolayer MoS_2 on sapphire and SiO_2. *Nano Res.* **2019**, *12*, 2646–2652.

[37] Shi, Y. Y.; Groven, B.; Serron, J.; Wu, X. Y.; Nalin Mehta, A.; Minj,

A.; Sergeant, S.; Han, H.; Asselberghs, I.; Lin, D. et al. Engineering wafer-scale epitaxial two-dimensional materials through sapphire template screening for advanced high-performance nanoelectronics. *ACS Nano* **2021**, *15*, 9482–9494.

[38] Li, L.; Wang, Q. Q.; Wu, F. F.; Xu, Q. L.; Tian, J. P.; Huang, Z. H.; Wang, Q. H.; Zhao, X.; Zhang, Q. H.; Fan, Q. K. et al. Epitaxy of wafer-scale single-crystal MoS_2 monolayer via buffer layer control. *Nat. Commun.* **2024**, *15*, 1825.

[39] Liu, L.; Li, T. T.; Ma, L.; Li, W. S.; Gao, S.; Sun, W. J.; Dong, R. K.; Zou, X. L.; Fan, D. X.; Shao, L. W. et al. Uniform nucleation and epitaxy of bilayer molybdenum disulfide on sapphire. *Nature* **2022**, *605*, 69–75.

[40] Fu, J. H.; Min, J. C.; Chang, C. K.; Tseng, C. C.; Wang, Q. X.; Sugisaki, H.; Li, C. Y.; Chang, Y. M.; Alnami, I.; Syong, W. R. et al. Oriented lateral growth of two-dimensional materials on *c*-plane sapphire. *Nat. Nanotechnol.* **2023**, *18*, 1289–1294.

[41] Lin, Y. C.; Jariwala, B.; Bersch, B. M.; Xu, K.; Nie, Y. F.; Wang, B. M.; Eichfeld, S. M.; Zhang, X. T.; Choudhury, T. H.; Pan, Y. et al. Realizing large-scale, electronic-grade two-dimensional semiconductors. *ACS Nano* **2018**, *12*, 965–975.

[42] Li, T. T.; Guo, W.; Ma, L.; Li, W. S.; Yu, Z. H.; Han, Z.; Gao, S.; Liu, L.; Fan, D. X.; Wang, Z. X. et al. Epitaxial growth of wafer-scale molybdenum disulfide semiconductor single crystals on sapphire. *Nat. Nanotechnol.* **2021**, *16*, 1201–1207.

[43] Wang, J. H.; Xu, X. Z.; Cheng, T.; Gu, L. H.; Qiao, R. X.; Liang, Z. H.; Ding, D. D.; Hong, H.; Zheng, P. M.; Zhang, Z. B. et al. Dual-coupling-guided epitaxial growth of wafer-scale single-crystal WS_2 monolayer on vicinal *a*-plane sapphire. *Nat. Nanotechnol.* **2022**, *17*, 33–38.

[44] Zhou, Z. J.; Hou, F. C.; Huang, X. L.; Wang, G.; Fu, Z. H.; Liu, W. L.; Yuan, G. W.; Xi, X. X.; Xu, J.; Lin, J. H. et al. Stack growth of wafer-scale van der Waals superconductor heterostructures. *Nature* **2023**, *621*, 499–505.

[45] Lee, C.; Yan, H. G.; Brus, L. E.; Heinz, T. F.; Hone, J.; Ryu, S. Anomalous lattice vibrations of single- and few-layer MoS_2. *ACS Nano* **2010**, *4*, 2695–2700.

[46] Wong, K. C.; Lu, X.; Cotter, J.; Eadie, D. T.; Wong, P. C.; Mitchell, K. A. R. Surface and friction characterization of MoS_2 and WS_2 third body thin films under simulated wheel/rail rolling-sliding contact. *Wear* **2008**, *264*, 526–534.

[47] Yang, Y.; Liang, Q. R.; Zhu, C. L.; Zheng, G. Z.; Zhang, J.; Zheng, S. J.; Lin, Y. C.; Zheng, D. Z.; Zhou, J. D. Chemical vapor deposition synthesis of V-doped MoS_2. *Rare Met.* **2023**, *42*, 3985–3992.

[48] Jeong, W.; Kim, T.; Kim, Y.; Jeong, M. S.; Kim, E. K. Improved characteristics of MoS_2 transistors with selective doping using 1,2-dichloroethane. *Semicond. Sci. Technol.* **2023**, *38*, 075013.

[49] Zhou, J. D.; Lin, J. H.; Huang, X. W.; Zhou, Y.; Chen, Y.; Xia, J.; Wang, H.; Xie, Y.; Yu, H. M.; Lei, J. C. et al. A library of atomically thin metal chalcogenides. *Nature* **2018**, *556*, 355–359.

[50] Xiong, J.; Wu, Q.; Cai, X. W.; Zhu, Y. M.; Lin, G. Y.; Li, C. Comparative study of sodium and potassium compounds as promoters for growth of monolayer MoS_2 with high crystal quality on SiO_2/Si substrate. *J. Phys. D: Appl. Phys.* **2024**, *57*, 405105.

[51] Chen, L.; Zang, L. Y.; Chen, L. H.; Wu, J. C.; Jiang, C. M.; Song, J. H. Study on the catalyst effect of NaCl on MoS_2 growth in a chemical vapor deposition process. *CrystEngComm* **2021**, *23*, 5337–5344.

[52] Weinberg, M. C.; Poisl, W. H.; Granasy, L. Crystal growth and classical nucleation theory. *C. R. Chim.* **2002**, *5*, 765–771.

[53] Dove, P. M.; Han, N. Z.; De Yoreo, J. J. Mechanisms of classical crystal growth theory explain quartz and silicate dissolution behavior. *Proc. Natl. Acad. Sci. USA* **2005**, *102*, 15357–15362.

[54] Wang, S. S.; Rong, Y. M.; Fan, Y.; Pacios, M.; Bhaskaran, H.; He, K.; Warner, J. H. Shape evolution of monolayer MoS_2 crystals grown by chemical vapor deposition. *Chem. Mater.* **2014**, *26*, 6371–6379.

[55] Chen, F.; Su, W. T.; Zhao, S. C.; Lv, Y. F.; Ding, S.; Fu, L. Morphological evolution of atomically thin MoS_2 flakes synthesized by a chemical vapor deposition strategy. *CrystEngComm* **2020**, *22*, 4174–4179.

[56] Li, X. Y.; Zhang, S. P.; Chen, S.; Zhang, X. L.; Gao, J. F.; Zhang, Y. W.; Zhao, J. J.; Shen, X.; Yu, R. C.; Yang, Y. et al. Mo concentration controls the morphological transitions from dendritic to semicompact, and to compact growth of monolayer crystalline MoS_2 on various substrates. *ACS Appl. Mater. Interfaces* **2019**, *11*, 42751–42759.

[57] Cao, Y. J.; Luo, X. F.; Han, S. M.; Yuan, C. L.; Yang, Y.; Li, Q. L.; Yu, T.; Ye, S. L. Influences of carrier gas flow rate on the morphologies of MoS_2 flakes. *Chem. Phys. Lett.* **2015**, *631–632*, 30–33.

[58] Park, T.; Bae, C.; Lee, H.; Leem, M.; Kim, H.; Ahn, W.; Kim, J.; Lee, E.; Shin, H.; Kim, H. Non-equilibrium fractal growth of MoS_2 for electrocatalytic hydrogen evolution. *CrystEngComm* **2019**, *21*, 478–486.

[59] van der Zande, A. M.; Huang, P. Y.; Chenet, D. A.; Berkelbach, T. C.; You, Y. M.; Lee, G. H.; Heinz, T. F.; Reichman, D. R.; Muller, D. A.; Hone, J. C. Grains and grain boundaries in highly crystalline monolayer molybdenum disulphide. *Nat. Mater.* **2013**, *12*, 554–561.

[60] Zhang, J.; Yu, H.; Chen, W.; Tian, X. Z.; Liu, D. H.; Cheng, M.; Xie, G. B.; Yang, W.; Yang, R.; Bai, X. D. et al. Scalable growth of high-quality polycrystalline MoS_2 monolayers on SiO_2 with tunable grain sizes. *ACS Nano* **2014**, *8*, 6024–6030.

[61] Wei, Z.; Tang, J.; Li, X. Y.; Chi, Z.; Wang, Y.; Wang, Q. Q.; Han, B.; Li, N.; Huang, B. Y.; Li, J. W. et al. Wafer-scale oxygen-doped MoS_2 monolayer. *Small Methods* **2021**, *5*, 2100091.

[62] Chen, W.; Zhao, J.; Zhang, J.; Gu, L.; Yang, Z. Z.; Li, X. M.; Yu, H.; Zhu, X. T.; Yang, R.; Shi, D. X. et al. Oxygen-assisted chemical vapor deposition growth of large single-crystal and high-quality monolayer MoS_2. *J. Am. Chem. Soc.* **2015**, *137*, 15632–15635.

[63] Tian, J. P.; Wang, Q. Q.; Huang, X. D.; Tang, J.; Chu, Y. B.; Wang, S. P.; Shen, C.; Zhao, Y. C.; Li, N.; Liu, J. Y. et al. Scaling of MoS_2 transistors and inverters to sub-10 nm channel length with high performance. *Nano Lett.* **2023**, *23*, 2764–2770.

[64] Jiang, J. F.; Xu, L.; Du, L. J.; Li, L.; Zhang, G. Y.; Qiu, C. G.; Peng, L. M. Yttrium-doping-induced metallization of molybdenum disulfide for ohmic contacts in two-dimensional transistors. *Nat. Electron.* **2024**, *7*, 545–556.